ADVANCED FUNCTIONAL MATERIALS
www.afm-journal.de

Highly Stable Two-Dimensional Tin(II) Iodide Hybrid Organic–Inorganic Perovskite Based on Stilbene Derivative

*In-Hyeok Park, Leiqiang Chu, Kai Leng, Yu Fong Choy, Wei Liu, Ibrahim Abdelwahab, Ziyu Zhu, Zhirui Ma, Wei Chen, Qing-Hua Xu, Goki Eda, and Kian Ping Loh**

Hybrid organic–inorganic perovskites have recently emerged as potential disruptive photovoltaic technology. However, the toxicity of lead used in state-of-the-art hybrid perovskites solar cell prevents large-scale commercialization, which calls for lead-free alternatives. Sn-based perovskites have been considered as alternatives but they are limited by rapid oxidation and decomposition in ambient air. Here, an Sn-based two-dimensional hybrid organic–inorganic perovskites $[A_2B_{(n-1)}Sn_nI_{(3n+1)}]$ (n = 1 and 2) are reported with improved air stability, using bulky stilbene derivatives as the organic cations (2-(4-(3-fluoro)stilbenyl)ethanammonium iodide (FSAI)). The moisture stability of the $[(FSA)_2SnI_4]$ perovskites is attributed to the hydrophobic properties of fluorine-functionalized organic chains (FSA), as well as the strong cohesive bonding in the organic chains provided by H bonds, CH···X type H bonds, weak interlayer F···F interaction, and weak face-to-face type π–π interactions. The photodetector device fabricated on exfoliated single crystal flake of $[(FSA)_2SnI_4]$ exhibits fast and stable photoconductor response.

1. Introduction

Hybrid organic–inorganic perovskites (HOIPs) have been intensively studied as materials for next generation optoelectronic devices due to their high absorption and good charge transport properties.[1] To date, they have shown outstanding performances in solar cells, light-emitting diodes, light detectors, as well as X-ray detectors.[2–7] For these next generation devices, lead-based HOIPs continues to be the material of choice due to their superior charge transport and light absorbing properties.[8–10] However, the possibility of toxic Pb^{2+} ions leeching from the perovskites in the presence of moisture hampers the commercialization of lead HOIPs. As a result, much effort has been dedicated to search for other alternatives, such as Sn and Bi etc.[11–13] Sn-based perovskites are attractive due to its higher conductivity, but it has the serious drawback of being chemically unstable due to the facile oxidation of tin(II) to tin(VI).[14–16] two-dimensional (2D) tin-based HOIPs are generally more stable than the 3D ones, thus there are increasing interests to apply them in photovoltaics. Recently, Loi's group have reported that 2D/3D mixed Sn perovskites solar cells exhibit an efficiency of 9%,[17] however the device was degraded in ambient air condition in 6 h.

In this paper, we investigated the use of large organic cations made of stilbene derivatives to generate new variants of Sn-based HOIPs. In particular, fluorine-functionalized stilbene derivatives show very good ambient and thermal stability on account of its interlayer and intralayer interactions. Photodetector fabricated from these perovskites exhibit fast and stable photoresponse.

2. Results and Discussions

2.1. Synthesis

2D organic–inorganic hybrid tin(II) iodide perovskites, $[A_2B_{(n-1)}Sn_nI_{(3n+1)}]$ (n = 1 and 2) based on bulky ammonium salts of stilbene derivatives were synthesized from reactions of tin(II) iodide, 2-(4-stilbenyl)ethanammonium iodide (SAI), 2-(4-(3-fluoro)stilbenyl)ethanammonium iodide (FSAI), and methylammonium iodide (**Figure 1**). Dark-red plate-shaped crystals of the tin(II) iodide stilbene perovskite (**TI-SP**) was obtained under solvothermal conditions by dissolving tin(II) iodide and SAI in a mixture of HI and ethanol (EtOH) at 90 °C, followed by slow cooling. By replacing SAI with FSAI, similar procedures were used to obtain dark-red plate-shaped crystals of tin(II) iodide fluorostilbene perovskite (**TI-FSP**) for single crystal X-ray diffraction (SC-XRD). To compare the stability of our synthesized perovskites with previously reported 2D Sn-based perovskites, dark-brown plate-shaped crystals of tin(II) iodide phenylethylamine perovskite (**TI-PEP**) incorporating phenylethylammonium iodide (PEAI), were synthesized using the reported procedure.[18] The purity and crystallinity of the bulk materials

Dr. I.-H. Park, Dr. L. Chu, Dr. K. Leng, Y. F. Choy, Dr. W. Liu, I. Abdelwahab, Z. Zhu, Z. Ma, Prof. W. Chen, Prof. Q.-H. Xu, Prof. G. Eda, Prof. K. P. Loh
Department of Chemistry
National University of Singapore
3 Science Drive 3, Singapore 117543, Singapore
E-mail: chmlohkp@nus.edu.sg
Dr. K. Leng, Prof. W. Chen, Prof. G. Eda, Prof. K. P. Loh
Centre for Advanced 2D Materials (CA2DM)
6 Science Drive 2, Singapore 117546, Singapore
Prof. W. Chen, Prof. G. Eda
Department of Physics
National University of Singapore
2 Science Drive 3, Singapore 117542, Singapore
The ORCID identification number(s) for the author(s) of this article can be found under https://doi.org/10.1002/adfm.201904810.

DOI: 10.1002/adfm.201904810

© 2019 WILEY-VCH Verlag GmbH & Co. KGaA, Weinheim

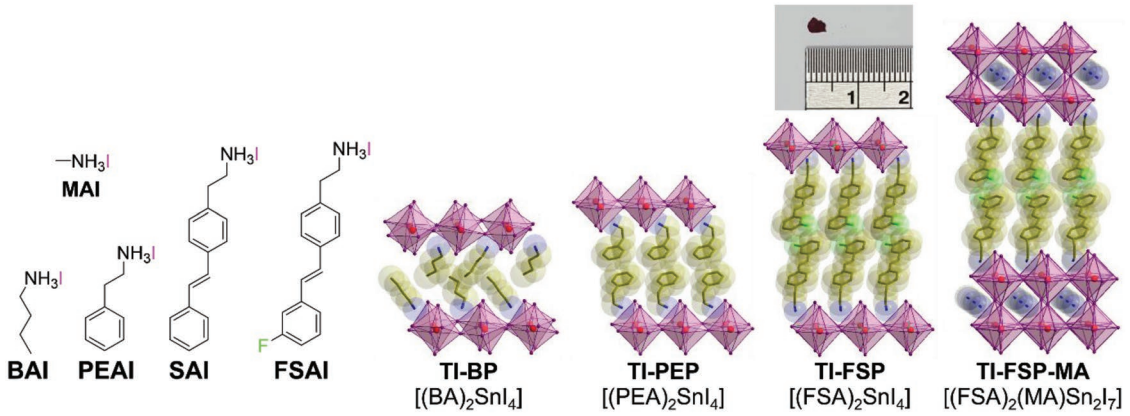

Figure 1. Chemical structures of the amine derivatives and their tin(II) iodide perovskites.

were confirmed by comparing the simulated powder X-ray diffraction (PXRD) patterns from the SC-XRD with the bulk materials (Figures S1 and S2, Supporting Information). Reported single crystal data of tin(II) iodide butylamine perovskite (**TI-BP**) was also used as a reference data for comparison.[19]

2.2. Optical Properties

Optical absorption and photoluminescence (PL) spectra of **TI-PEP**, **TI-SP**, **TI-FSP**, and **TI-FSP-MA** were recorded using 532 nm laser excitation at room temperature and at 77 K (**Figure 2** and Figures S15–18, Supporting Information). Sharp excitonic features could be observed for all four crystals, attesting to their crystalline quality. Compared to the lead-based counterparts, the Sn-based perovskites of the similar class typically have smaller optical gaps and hence PL emissions usually occur at wavelengths longer than 600 nm. Interestingly, the presence of F atoms in the organic moieties buckles the trend and blue-shift the PL emission for the $n = 1$ homologue.

Optical absorption of **TI-SP** shows an exciton peak at 594 nm, while **TI-PEP** shows an absorption peak at 603 nm. The optical

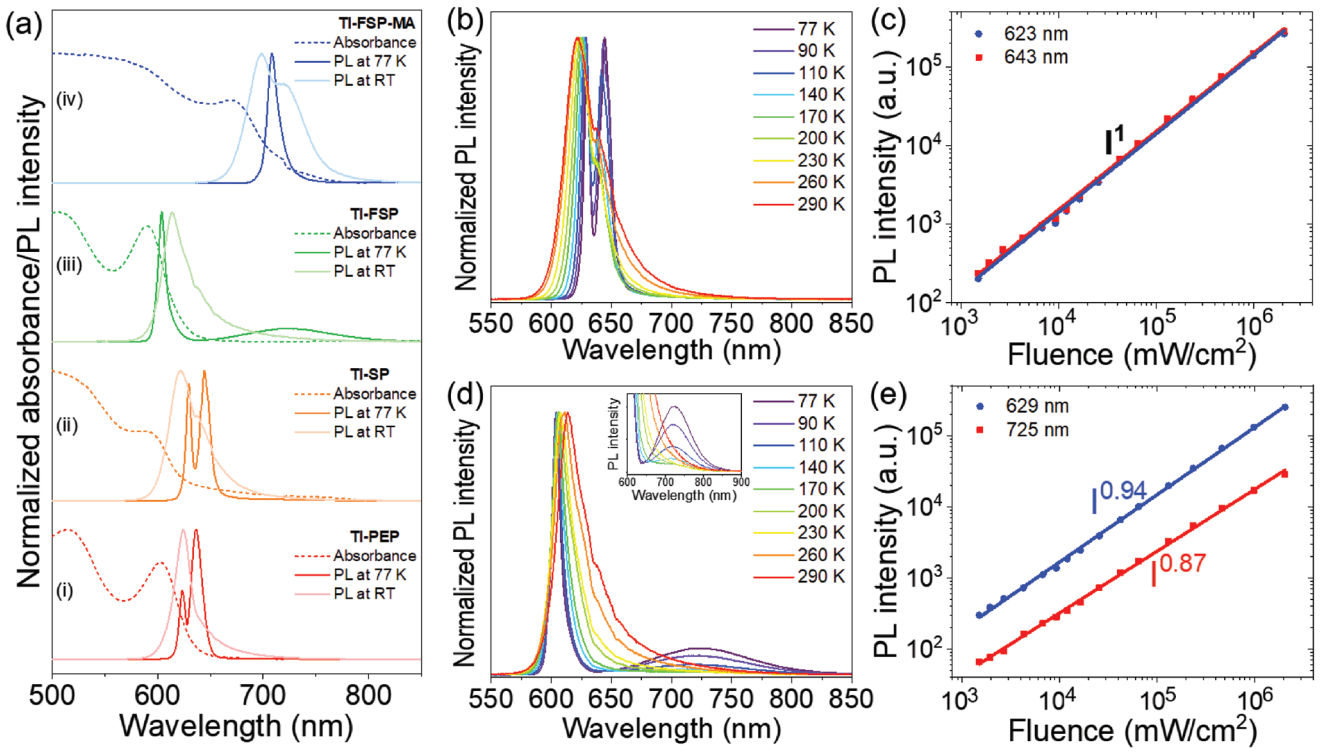

Figure 2. a) Optical absorbance and PL spectra for i) **TI-PEP**, ii) **TI-SP**, iii) **TI-FSP**, and iv) **TI-FSP-MA** at room temperature and 77 K (excitation at 532 nm). Spin-coated films on quartz substrates were used for the optical absorbance measurements. b) Temperature-dependent normalized PL intensity for **TI-SP** from 77 to 290 K. c) Excitation power-dependent peak intensities for **TI-SP**. d) Temperature-dependent normalized PL intensity for **TI-FSP** from 77 to 290 K. e) Excitation fluence-dependent peak intensities for **TI-FSP**.

© 2019 WILEY-VCH Verlag GmbH & Co. KGaA, Weinheim

absorption of **TI-PEP** at room temperature agrees with previous reports.[20,21] The room temperature PL of tin-based perovskites exhibit Stokes shifts in this sequence: 21 nm for **TI-PEP** ($\lambda_{em\text{-}max}$ at 624 nm), 27 nm for **TI-SP** ($\lambda_{em\text{-}max}$ at 621 nm), 23 nm for **TI-FSP** ($\lambda_{em\text{-}max}$ at 613 nm), and 25 nm for **TI-FSP-MA** ($\lambda_{em\text{-}max}$ at 673 nm). At 77 K, **TI-PEP** and **TI-SP** show two red-shifted emission peaks (**TI-PEP** at 623 and 636 nm; **TI-SP** at 629 and 645 nm); these spectral redshifts are similar to what had been reported for lead(II) iodide phenylethylamine perovskite (**LI-PEP**).[22] The temperature-dependent PL results of **TI-SP** and **TI-PEP** is quite similar, so here we focus our discussion on **TI-SP**. The higher energy PL peak in Figure 2b is assigned to free exciton emissions and the low-energy peak to 2D localized and self-trapped excitons. The excitonic features of the two peaks are also confirmed by the fluence-dependent PL intensity studies in Figure 2c, where the peak intensities show linear dependence on the fluence. In addition, the asymmetric feature for the low-energy peak spectra could result from disorder induced broadening of the low-energy tail. The two PL peaks blue-shift with increasing temperature, which may be due to thermally induced lattice expansion, as has been observed previously for some classes of lead-based perovskites.[23,24] The increasing linewidth of the lower energy peak with increasing temperature is due to exciton-phonon interaction. The excitonic origins of the high- and low-energy PL peaks were confirmed from laser fluence-dependent PL studies, where a linear behavior of the PL intensity with laser fluence was observed across three orders of laser power. In addition, the continuous evolution of the PL spectra with temperature, as opposed to a sharper change expected for the phase transition, suggests that phase change does not play a major role in influencing the peak evolution here.

The temperature-dependent PL spectra of **TI-FSP** are shown in Figure 2d,e. Unlike **TI-PEP** and **TI-SP**, the PL spectrum of **TI-FSP** is dominated by a single excitonic peak at 603 nm at 77 K, along with a broad feature around 725 nm due to defects. These features are also reflected in the fluence-dependent PL intensities displayed in Figure 2e. The high-energy peak intensity exhibits a power dependence value around 1, while the broad low-energy peak intensity shows sublinear dependence with fluence, a sign of saturated disordered emission states. Meanwhile, with increasing temperature, emission from defects also diminishes due to thermal excitation and increased non-radiative recombination. The main excitonic peak broadens considerably and redshifts with increasing temperatures, suggesting the presence of much stronger dynamic disorder and lattice anharmonicity as compared to **TI-SP** and **TI-PEP**. In the PL spectrum of **TI-FSP-MA**, the two emission peaks at 698 and 722 nm observed at room temperature merges into one emission peak at 708 nm at 110 K (Figure S22, Supporting Information). This could be due to the ordering of the MA molecules inside the $[Sn_2I_7]^{3-}$ layer as the temperature is reduced.[25]

2.3. Single Crystal X-ray Structural Descriptions

SC-XRD analysis of $[(FSA)_2SnI_4]$ (known hereafter as **TI-FSP**) at two different temperatures (293 and 100 K) was performed to investigate structural phase change as a function of temperature (**Figure 3** and Table S1, Supporting Information). **TI-FSP** is an isoreticular structure with **TI-BP** and **TI-PEP**. The building block of **TI-FSP** is mainly a well-ordered $[SnI_4]^{2-}$ layer of corner-sharing octahedron $[SnI_6]$ unit terminated by FSA cations on top and bottom sides of the anionic cage. The NH_3 of FSA cations are hydrogen bonded to I atoms of the $[SnI_4]^{2-}$ inorganic layer. SC-XRD of **TI-FSP** reveals that its space group is triclinic *P*-1 at room temperature, and changes to monoclinic $C2/m$ at low temperature. At 293 K, the asymmetric unit contains two half Sn^{II} atoms, two I anions and two half FSA molecules (Figure 3A-a). Interestingly, the presence of the olefin bonds in the stilbene structure allows pedal motion: two conformers of FSA induced by the conformational interconversion of the olefin bonds[19] were observed in **TI-FSP** at room temperature (Figure 3A-a). This is the basis of dynamic disorder, however the asymmetric unit of **TI-FSP** at 100 K decreases to half of those of **TI-FSP** at room temperature, as it now contains one quarter Sn^{II} atom, one I atom and one half FSA molecules (Figure 3B-a). The FSA molecules in **TI-FSP** are disordered in terms of olefin-based conformation at room temperature but not at 100 K (Figures S12 and S13, Supporting Information). The FSA molecules and iodine atoms in **TI-FSP** are disordered in terms of molecule/atom positions at both temperatures. Such a temperature-dependent dynamic disorder gives rise to the PL broadening observed in Figure 2d for **TI-FSP**.

Due to the layer-by-layer segregation of organic and inorganic components in hybrid perovskites, the organic cation chains play important roles in imparting stability on the hybrid perovskites, and the degree of stabilization depends on the compactness of its packing as well as its chemical reactivity. The hydrophobicity of FSA imbues **TI-FSP** with moisture resistance, thus it is more stable than **TI-PEP** in ambient air. The stability of **TI-FSP** can be rationalized on the basis of its packing structure. As shown in Figure 3C, the organic PEA molecules in **TI-PEP** have only weak interchain hydrophobic interactions (Figure 3C-b), and there are void spaces between the PEA molecules (violet colored iodide atoms) that allows infiltration by water molecules. In contrast, the FSA molecules in TI-FSP possess two aromatic rings and are stacked by π–π interactions (Figure 3C-c). Additional supramolecular interactions in **TI-FSP**, which include CH···X type H bonds,[26] interlayer F···F interaction,[27] and weak face-to-face type Π-Π interactions, augment the cohesive forces between FSA molecules and make a water-resistant compact layer. As a counter example, the loose packing structure of **TI-BP** results in it being the least stable among all (Figure 3C-a).

It is known that controlling the number of inorganic layers in the Sn-based perovskites $(BA)_2(MA)_{n-1}Sn_nI_{3n+1}$ (n = 1–5) allows the conductivity of Sn-based perovskite to be tuned from semiconducting to metallic behavior.[14] We have successfully prepared the n = 2 homologue by incorporating MA molecules. Preparation of higher homologue with formula $[(FSA)_2(MA)Sn_2I_7]$ (abbreviated as **TI-FSP-MA**) is challenging because of the large difference in solubility of the bulky organic molecule FSA and tiny organic molecule MA). SC-XRD analysis of **TI-FSP-MA** was performed to confirm the structural phase change (**Figure 4** and Table S1, Supporting Information). **TI-FSP-MA** shows temperature-dependent phase change from triclinic space group *P*-1 at 293 K to monoclinic space group $C2/m$ at 100 K (Figure 4 and

© 2019 WILEY-VCH Verlag GmbH & Co. KGaA, Weinheim

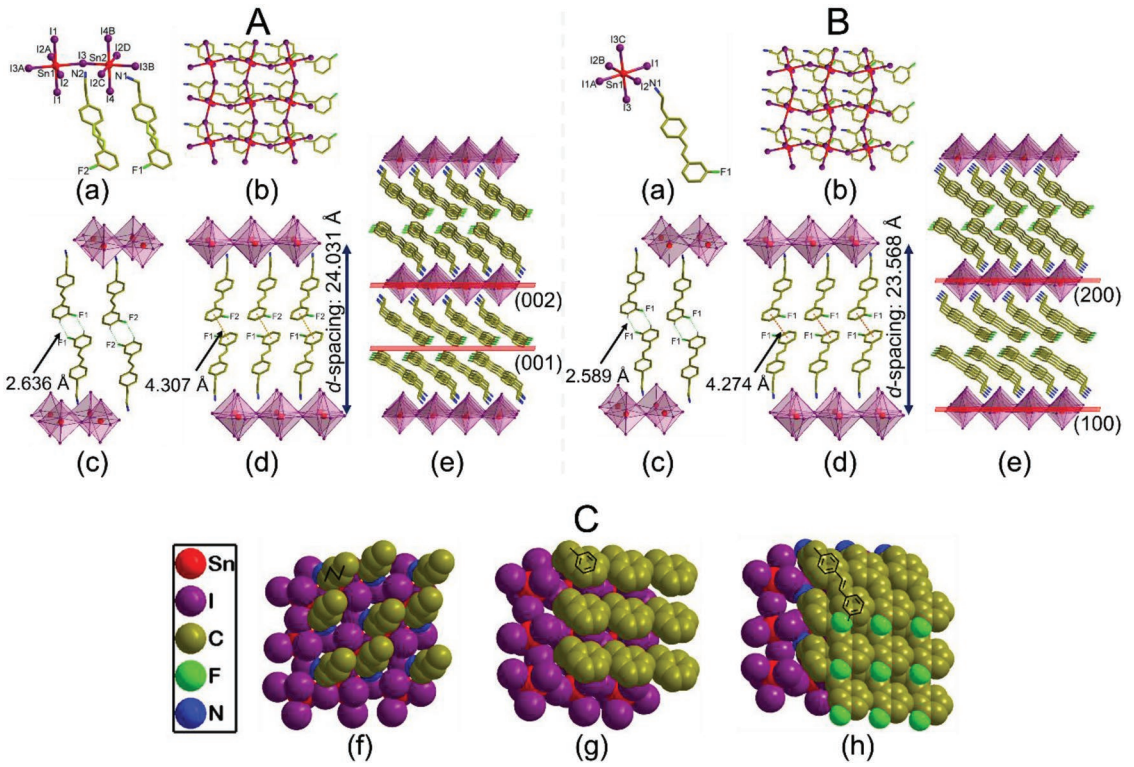

Figure 3. Structural comparison of single crystal structure of tin(II) iodide fluorostilbene perovskite (**TI-FSP**, $n = 1$), $[(FSA)_2SnI_4]$ at A) room temperature (293 K) and at B) low temperature (100 K). a) Core unit of Sn(II) and FSA. Symmetry codes (left, A) at room temperature phase for A): $-1-x, -1-y, 1-z$; B): $-x, -y, 1-z$; C): $-1-x, -y, 1-z$; D): $1+x, y, z$ and (right, B) at low-temperature phase for A): $1-x, 1+y, 1-z$; B): $x, y, 1+z$; C): $1-x, y, 1-z$. b) A view of single layer $[SnI_4]^{2-}$ with organic cations. c) The CH···X type H bonds from adjacent FSA molecules between organic layers. d) Weak π–π interactions of organic layers between $[SnI_4]^{2-}$ inorganic layers with *d*-spacing. e) 2D layered packing structure showing oriented crystallographic planes. C) Structural comparison of single crystal structure of f) **TI-BP**, g) **TI-PEP**, and h) **TI-FSP** showing packing mode with space-filling view of inorganic layer and nine organic molecules. Hydrogen atoms are not shown for clarity.

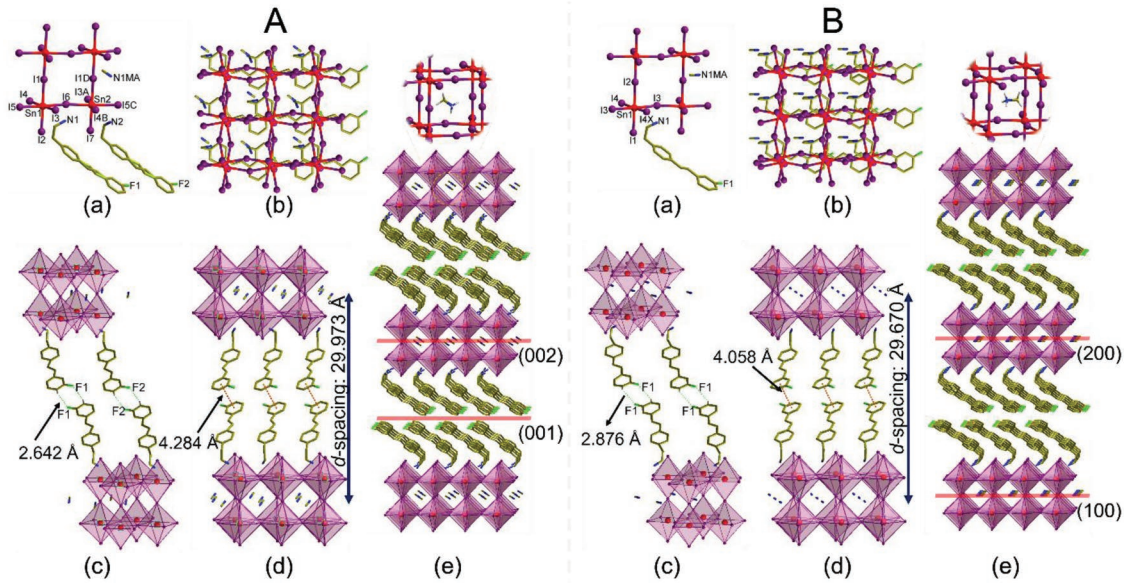

Figure 4. Structural comparison of single crystal structure of tin(II) iodide fluorostilbene/MA perovskite (**TI-FSP-MA**, $n = 2$), $[(FSA)_2(MA)Sn_2I_7]$ at A) room temperature (293 K) and at B) low temperature (100 K). a) Core unit of Sn(II) and FSA. b) A view of single layer $[SnI_4]^{2-}$ with organic cations. c) Weak π–π interactions of organic layers between $[SnI_4]^{2-}$ inorganic layers with *d*-spacing. d) Weak π–π interactions of organic layers between $[SnI_4]^{2-}$ inorganic layers with *d*-spacing. e) 2D layered packing structure showing oriented crystallographic planes. Symmetry codes (left, A) at room temperature phase for A): $x, 1+y, z$; B): $-1+x, y, z$; C): $-1+x, 1+y, z$; D): $1-x, 1-y, -z$. The hydrogen atoms and disordered parts from I atoms and FSA molecules are not shown for clarity.

 © 2019 WILEY-VCH Verlag GmbH & Co. KGaA, Weinheim

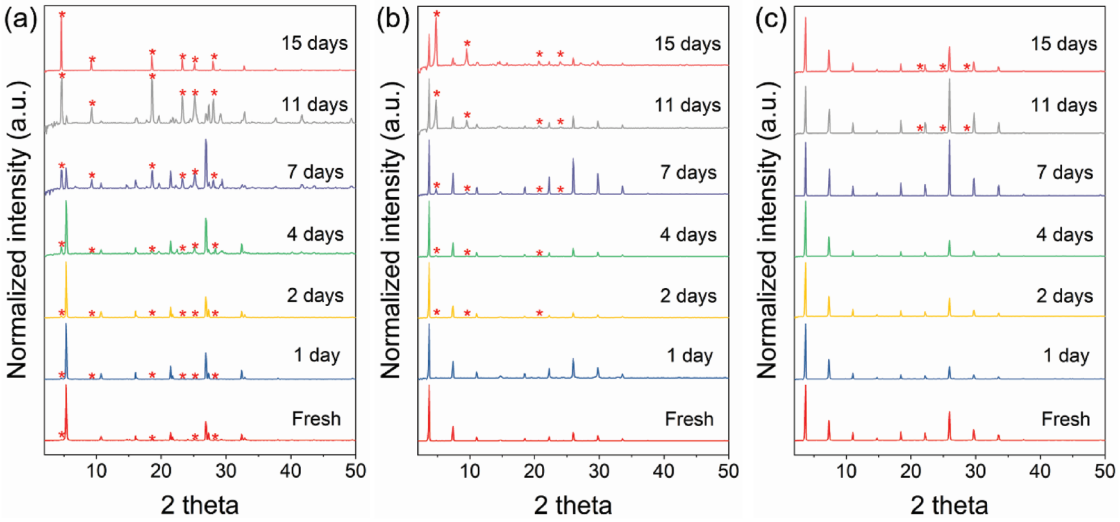

Figure 5. Air-stability of tin(II) iodide perovskites: comparison of PXRD patterns of a) **TI-PEP**, b) **TI-SP**, and c) **TI-FSP** for the fresh perovskites and after exposure to ambient condition at 60% RH for up to 15 d (*: oxidized products).

Table S1, Supporting Information). Same as **TI-FSP**, the FSA molecules in **TI-FSP-MA** are disordered in terms of olefin-based conformation at room temperature but not at 100 K (Figure 4a). The FSA molecules and iodine atoms in **TI-FSP-MA** are disordered in terms of molecule/atom positions at both temperatures (Figures S16 and S17, Supporting Information). In MA molecule in **TI-FSP-MA** at both temperature, the MA molecules are disordered over two positions at room temperature. Similar to **TI-FSP**, the packing structure of **TI-FSP-MA** are structurally stabilized by H bonds, $CH_3\cdots X$ type H bonds, $CH\cdots X$ type H bonds, weak interlayer $F\cdots F$ interaction, and weak face-to-face type π-π interactions. In accordance with the reduced bandgap of the higher homologues, **TI-FSP-MA** shows an absorption maxima at 673 nm. At 77 K, it has a single PL peak at 708 nm, which splits into two peaks at room temperature.

2.4. Stability

We have investigated the air, water, photo- and thermal stability of single crystals of the tin(II)-based perovskites **TI-PEP**, **TI-SP**, and **TI-FSP** using PXRD, PL, and thermogravimetric analysis (TGA), respectively (**Figure 5**). One of the significant problems of tin(II)-based perovskites is their severe air-instability originating from rapidly oxidation of Sn(II) to Sn(IV) when exposed in air due to the oxygen.[28,29] Hence, we tested the air stability of these three perovskites (up to 15 d) by monitoring changes in PXRD spectra as a function of air exposure time (Figure 5a–c). The PXRD peaks of **TI-FSP** remain unchanged throughout the duration of air exposure at 60% relative humidity (RH), which attests to its stability against oxidation. In contrast to relatively constant PXRD signals for TI-FSP, we found that as-prepared **TI-PEP** already showed three extra PXRD peaks at 4.7°, 18.6°, and 28.1° due to oxidation; a new peak was observed at 9.3° after exposing to ambient air at 60% RH for 1 d. As a function of time exposure, the intensity of the original peaks from fresh **TI-PEP** decreased and the intensity of the extra peaks associated with oxidized products increased. After 15 d, only the oxidized peaks remained. In the case of **TI-SP**, the decomposed/oxidized peaks appeared at 4.8°, 9.5°, and 20.6° after 2 d (Figure 5b). After 7 d, a new peak of **TI-SP** was also observed at 24.0°. It is well known that B-γ$CsSnI_3$ is oxidized to a Sn(IV) salt with the formula of Cs_2SnI_6 in ambient air.[30] Simulating the PXRD peaks for air-exposed **TI-FSP** suggest that the new peaks can be attributed to oxidized Sn(IV) salts with formulae $(amine)_4Sn^{IV}I_8$ and $Sn^{IV}O_2$ (Figure S27, Supporting Information). Thus, the absence of Sn(IV)-related PXRD peaks in **TI-FSP** suggest that it is relatively air stable, and the bulk of the crystal remains unoxidized.

The stability of **TI-FSP** in water was compared with **TI-PEP** by immersion in water (Figure S10, Supporting Information). In general, HOIPs were decomposed immediately when immersed in water. The brown crystals of **TI-PEP** turned yellow upon contact with water. In contrast, **TI-FSP** was found to be stable in water for 60 min or more. After 80 min, the surface color of the crystal began to change to a pale white.

The photostability of the perovskite crystal is an important performance metric in optoelectronic devices. Previous reports on the PL properties of Sn-based perovskites are rare, we suspect that this is to be due to the photo-instability of Sn-based perovskites. To test the stability of the crystal when irradiated by a laser in air, the PL spectra of tin-based perovskites that were exposed to 24 mW laser was recorded as a function of laser irradiation time (Figure S6, Supporting Information). The PL intensity of **TI-PEP** was quenched by 80% after 18 min of laser irradiation (Figure S6a, Supporting Information). In contrast, both **TI-SP** (Figure S6b, Supporting Information) and **TI-FSP** (Figure S6c, Supporting Information) show a stronger resistance to photo-degradation, for example, the PL intensity of **TI-FSP** was only quenched by 10% after 15 min of continuous laser irradiation in air.

To monitor the thermal stability of the tin(II)-based perovskites **TI-PEP**, **TI-SP**, and **TI-FSP**, TGA and differential scanning calorimetry (DSC) were measured under N_2 flow (Figures S5 and S6 and Table S2, Supporting Information). As shown in Figure S7a in the Supporting Information, the degradation of PEA and

© 2019 WILEY-VCH Verlag GmbH & Co. KGaA, Weinheim

dehalogenation of **TI-PEP** started near 165 °C. **TI-SP** is thermally stable up to 250 °C (Figure S7b, Supporting Information). The decomposition onset of **TI-FSP** occurs at a much higher temperature of 260 °C (Figure S7c, Supporting Information). Two main transitions T_s (structural transition) and T_m (melting transition) can be seen in the DSC curves of **TI-PEP**, **TI-SP**, and **TI-FSP** (Figure S8, Supporting Information). These transitions are similar to what had been reported for Pb- and Sn-based perovskites.[31,32] Compared to T_m of **TI-PEP**, the T_m of **TI-SP** and **TI-FSP** were observed at higher temperatures (278.5 and 272.5 °C, respectively). The thermal stability of metal iodide perovskite depends on the ease of forming the decomposed product HI, which is related to the acidity of the organic cations.[33] Therefore it is confirmed that the air stability, photostability, and thermal stability of our tin-based perovskites are significantly enhanced as compared to perovskites lacking the fluorostilbene moiety.

Another critical test of stability is examining at the chemical stability of the exfoliated flakes, since it is recognized that ultrathin flakes are usually less stable than the bulk crystals. Bulk crystals of **TI-PEP**, **TI-SP**, and **TI-FSP** were mechanically exfoliated onto clean Si/SiO_2 substrates using the scotch-tape method reported for graphene inside a glove box filled with inert gas (**Figure 6**a–f).[34]

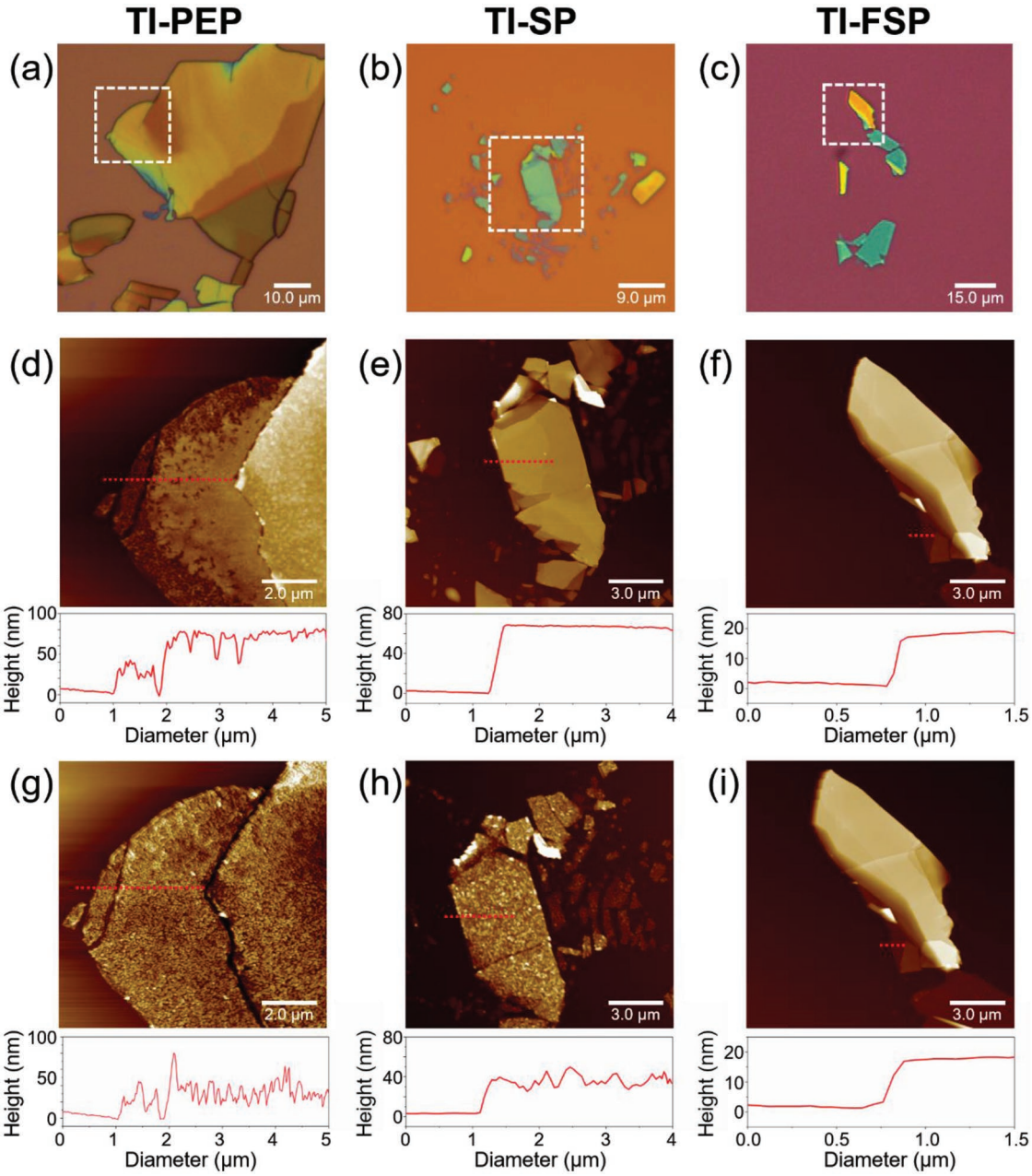

Figure 6. Optical images of a) **TI-PEP**, b) **TI-SP**, and c) **TI-FSP**. Time-dependent stability of exfoliated, tin-based perovskites multilayers prepared by the scotch-tape method from their bulk single crystals AFM images and corresponding height profiles of the exfoliated flakes of d) **TI-PEP**, e) **TI-SP**, and f) **TI-FSP;** and after exposure in ambient condition for g) 6 h, h) 24 h, and i) 24 h, respectively.

© 2019 WILEY-VCH Verlag GmbH & Co. KGaA, Weinheim

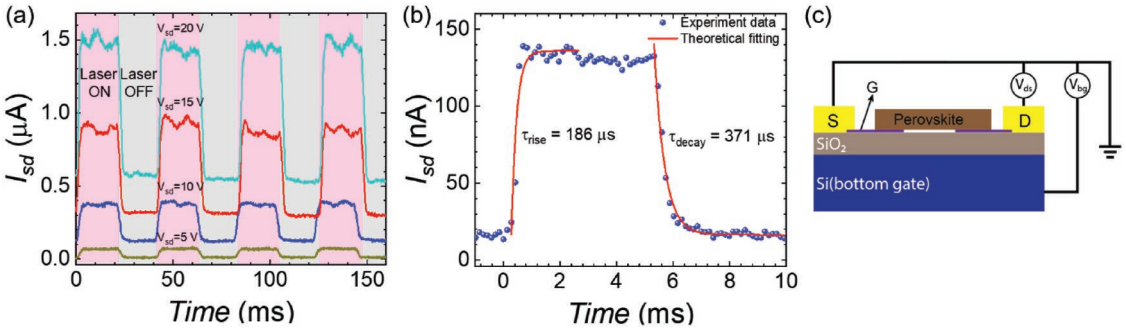

Figure 7. Photocurrent measurement of exfoliated flake of TI-FSP at 77 K. a) Time-resolved photoresponse of the device at a laser power P_{inc} = 1.14 mW, recorded at different value of bias voltages V_{sd}. The photocurrent signal was monitored with a chopper in the optical pass with a frequency of 25 Hz. b) Time-resolved photocurrent response with estimated rise time of 186 μs and decay time of 371 μs. The red curves are theoretical fittings to the experimental data using a single exponential function. c) A schematic illustration of the device structure for the photo-FET device.

These exfoliated flakes were subsequently removed from the glove box and exposed to air. Atomic force microscopy (AFM) was then used to monitor surface stability of the exfoliated thin flakes in ambient condition. In the case of **TI-PEP**, we observed that the degradation of edges occurred soon after air-exposure (Figure 6e). Flakes exfoliated from **TI-PEP** were completely degraded after 6 h of exposure in ambient condition (Figure 6g). After 24 h of exposure, thin flake of **TI-SP** also shows signs of decomposition, as can be judged from the increasingly rough morphology and reduced height profile (from 66 to 34 nm, Figure 6h). In contrast, the exfoliated flake of **TI-FSP** shows smooth and unchanging surface morphology throughout the air exposure (Figure 6g, i).

We monitored the surface stability of **TI-PEP**, **TI-FSP**, **TI-FSP-MA** by near ambient pressure X-ray photoelectron spectroscopy (XPS) under 0.7 bar oxygen condition. After 2 h of similar exposure condition to O_2, the oxidized Sn^{4+} component in the convoluted XPS spectra of **TI-PEP**, **TI-FSP**, and **TI-FSP-MA** were observed to be 73.3%, 39.6%, and 45.4%, respectively. It is clear that **TI-FSP** shows better oxygen stability compared to **TI-PEP**. XPS signal has a depth origin that are typically less than 20 nm. The presence of the oxidized component is mainly due to the ability of O_2 to infiltrate the interchain space in the organic layers at the surface region, the bulk however remains unoxidized as judged from the absence of Sn(IV)-related oxidized species in PXRD pattern.

2.5. Photocurrent Response

The air-stability of **TI-FSP** allows us to fabricate photo-FET (field effect transistor) devices without worrying about exposing the sample to the ambient during transfer between measurement systems. In order to characterize the photocurrent response properties of the material, we fabricated FET device on **TI-FSP**. We exfoliated the crystal onto polydimethylsiloxane and a uniform perovskite flake was then selected and transferred to pre-pattered carbon electrodes on a highly p-doped silicon substrate with 285 nm thick thermal SiO_2 dielectric layer (Figure S24, Supporting Information). To extract the intrinsic electronic property, photocurrent measurement was all performed in vacuum condition to avoid any air doping effects.

Figure 7a shows the time-resolved photocurrent recorded at four different V_{sd} values, with a 532 nm incident laser of power P_{inc} = 1.14 mW. The photocurrent signal was monitored with a chopper in the optical pass with a frequency of 25 Hz. The fast photoresponse implies efficient charge separation and collection at the graphene/perovskite interface.[35] Figure 7b shows the temporal photocurrent response of the device. The rise and decay time are estimated to be about τ_{rise} = 186 μs and τ_{decay} = 371 μs, with the rising and falling part of the curve fitted using a single exponential function. The response time is better than most 2D materials and their heterostructures,[36] indicating our Sn-based perovskite phototransistor can be used as a fast and sensitive optical switching device.

3. Conclusion

In summary, we have synthesized Sn-based 2D HOIPs, $[A_2B_{(n-1)}Sn_nI_{(3n+1)}]$ (n = 1 and 2), using bulky stilbene derivatives as the organic cations (FSAI). The fluorine substituent is found to improve the stability of the Sn-based perovskites due to a more compact packing of the organic cations, mediated by usual H bonds common to 2D perovskites, and augmented by special face-to-face π–π interactions, CH···X type H bonds, and interlayer F···F interactions. As a result, our Sn-based 2D perovskite crystal shows much better air and water stability than previously reported Sn-based counterparts. Photodetector fabricated on flakes exfoliated from bulk **TI-FSP** crystals show fast and stable photoresponse. Our studies show that proper design of organic cations can extend the stability lifetime of Sn-based perovskites, and stimulate more research into Pb-free alternatives for device applications.

Supporting Information

Supporting Information is available from the Wiley Online Library or from the author.

Acknowledgements

I.-H.P and L.C. contributed equally to this work. This work was supported by A* STAR–DST funding under the project "Flexible and

© 2019 WILEY-VCH Verlag GmbH & Co. KGaA, Weinheim

High Performance Based Perovskite Solar Cells on Graphene, A/C No: R-143000-598-305. I.-H.P. thanks to Overseas Postdoctoral Fellowship of Foresting Next-Generation Research Program through National Research Foundation of Korea (2017R1A6A3A03006579).

Conflict of Interest

The authors declare no conflict of interest.

Keywords

2D material, hybrid perovskite, stability, stilbene, tin(II) iodide

Received: June 15, 2019
Revised: July 9, 2019
Published online: August 5, 2019

[1] B. Saparov, D. B. Mitzi, *Chem. Rev.* **2016**, *116*, 4558.
[2] N. J. Jeon, J. H. Noh, W. S. Yang, Y. C. Kim, S. Ryu, J. Seo, S. I. Seok, *Nature* **2015**, *517*, 476.
[3] W. S. Yang, J. H. Noh, N. J. Jeon, Y. C. Kim, S. Ryu, J. Seo, S. I. Seok, *Science* **2015**, *348*, 1234.
[4] H. Tsai, W. Nie, J.-C. Blancon, C. C. Stoumpos, R. Asadpour, B. Harutyunyan, A. J. Neukirch, R. Verduzco, J. J. Crochet, S. Tretiak, L. Pedesseau, J. Even, M. A. Alam, G. Gupta, J. Lou, P. M. Ajayan, M. J. Bedzyk, M. G. Kanatzidis, A. D. Mohite, *Nature* **2016**, *536*, 312.
[5] M. A. Green, A. Ho-Baillie, H. J. Snaith, *Nat. Photonics* **2014**, *8*, 506.
[6] J.-H. Im, I.-H. Jang, N. Pellet, M. Grätzel, N.-G. Park, *Nat. Nanotechnol.* **2014**, *9*, 927.
[7] H. Cho, S.-H. Jeong, M.-H. Park, Y.-H. Kim, C. Wolf, C.-L. Lee, J. H. Heo, A. Sadhanala, N. Myoung, S. Yoo, S. H. Im, R. H. Friend, T.-W. Lee, *Science* **2015**, *350*, 1222.
[8] M. Yuan, L. N. Quan, R. Comin, G. Walters, R. Sabatini, O. Voznyy, S. Hoogland, Y. Zhao, E. M. Beauregard, P. Kanjanaboos, Z. Lu, D. H. Kim, E. H. Sargent, *Nat. Nanotechnol.* **2016**, *11*, 872.
[9] W. S. Yang, B.-W. Park, E. H. Jung, N. J. Jeon, Y. C. Kim, D. U. Lee, S. S. Shin, J. Seo, E. K. Kim, J. H. Noh, S. I. Seok, *Science* **2017**, *356*, 1376.
[10] K. Leng, I. Abdelwahab, I. Verzhbitskiy, M. Telychko, L. Chu, W. Fu, X. Chi, N. Guo, Z. Chen, Z. Chen, C. Zhang, Q.-H. Xu, J. Lu, M. Chhowalla, G. Eda, K. P. Loh, *Nat. Mater.* **2018**, *17*, 908.
[11] Z. Shi, J. Guo, Y. Chen, Q. Li, Y. Pan, H. Zhang, Y. Xia, W. Huang, *Adv. Mater.* **2017**, *29*, 1605005.
[12] F. Hao, C. C. Stoumpos, D. H. Cao, R. P. H. Chang, M. G. Kanatzidis, *Nat. Photonics* **2014**, *8*, 489.
[13] W. Ke, C. C. Stoumpos, I. Spanopoulos, L. Mao, M. Chen, M. R. Wasielewski, M. G. Kanatzidis, *J. Am. Chem. Soc.* **2017**, *139*, 14800.
[14] D. B. Mitzi, C. A. Feild, W. T. A. Harrison, A. M. Guloy, *Nature* **1994**, *369*, 467.
[15] C. R. Kagan, D. B. Mitzi, C. D. Dimitrakopoulos, *Science* **1999**, *286*, 945.
[16] D. B. Mitzi, S. Wang, C. A. Feild, C. A. Chess, A. M. Guloy, *Science* **1995**, *267*, 1473.
[17] S. Shao, J. Liu, G. Portale, H.-H. Fang, G. R. Blake, G. H. ten Brink, L. J. A. Koster, M. A. Loi, *Adv. Energy Mater.* **2018**, *8*, 1702019.
[18] G. C. Papavassiliou, J. B. Koutselas, D. J. Lagouvardos, *Z. Naturfor. B* **1993**, *48*, 1013.
[19] D. B. Mitzi, *Chem. Mater.* **1996**, *8*, 791.
[20] M.-Y. Chen, J.-T. Lin, C.-S. Hsu, C.-K. Chang, C.-W. Chiu, H. M. Chen, P.-T. Chou, *Adv. Mater.* **2018**, *30*, 1706592.
[21] Y. Liao, H. Liu, W. Zhou, D. Yang, Y. Shang, Z. Shi, B. Li, X. Jiang, L. Zhang, L. N. Quan, R. Quintero-Bermudez, B. R. Sutherland, Q. Mi, E. H. Sargent, Z. Ning, *J. Am. Chem. Soc.* **2017**, *139*, 6693.
[22] L. Gan, H. He, S. Li, J. Li, Z. Ye, *J. Mater. Chem. C* **2016**, *4*, 10198.
[23] H.-H. Fang, S. Adjokatse, S. Shao, J. Even, M. A. Loi, *Nat. Commun.* **2018**, *9*, 243.
[24] M. I. Dar, G. Jacopin, S. Meloni, A. Mattoni, N. Arora, A. Boziki, S. M. Zakeeruddin, U. Rothlisberger, M. Grätzel, *Sci. Adv.* **2016**, *2*, e1601156.
[25] H.-H. Fang, R. Raissa, M. Abdu-Aguye, S. Adjokatse, G. R. Blake, J. Even, M. A. Loi, *Adv. Funct. Mater.* **2015**, *25*, 2378.
[26] D. B. Mitzi, C. D. Dimitrakopoulos, L. L. Kosbar, *Chem. Mater.* **2001**, *13*, 3728.
[27] G. R. Desiraju, R. Parthasarathy, *J. Am. Chem. Soc.* **1989**, *111*, 8725.
[28] A. Abate, *Joule* **2017**, *1*, 659.
[29] L. Liang, P. Gao, *Adv. Sci.* **2018**, *5*, 1700331.
[30] K. P. Marshall, M. Walker, R. I. Walton, R. A. Hatton, *Nat. Energy* **2016**, *1*, 16178.
[31] T. Li, W. A. Dunlap-Shohl, Q. Han, D. B. Mitzi, *Chem. Mater.* **2017**, *29*, 6200.
[32] D. B. Mitzi, D. R. Medeiros, P. W. DeHaven, *Chem. Mater.* **2002**, *14*, 2839.
[33] J. Yang, B. D. Siempelkamp, E. Mosconi, F. De Angelis, T. L. Kelly, *Chem. Mater.* **2015**, *27*, 4229.
[34] I. Abdelwahab, G. Grinblat, K. Leng, Y. Li, X. Chi, A. Rusydi, S. A. Maier, K. P. Loh, *ACS Nano* **2018**, *12*, 644.
[35] H. Hong, J. Zhang, J. Zhang, R. Qiao, F. Yao, Y. Cheng, C. Wu, L. Lin, K. Jia, Y. Zhao, Q. Zhao, P. Gao, J. Xiong, K. Shi, D. Yu, Z. Liu, S. Meng, H. Peng, K. Liu, *J. Am. Chem. Soc.* **2018**, *140*, 14952.
[36] S. Zhao, J. Wu, K. Jin, H. Ding, T. Li, C. Wu, N. Pan, X. Wang, *Adv. Funct. Mater.* **2018**, *28*, 1802011.

© 2019 WILEY-VCH Verlag GmbH & Co. KGaA, Weinheim